IOP Publishing

Plasma Sources Science and Technology

Plasma Sources Sci. Technol. **32** (2023) 025003 (18pp)

https://doi.org/10.1088/1361-6595/acb813

A numerical and experimental study on positive diffusive ionization waves in different N_2/O_2 mixtures: the role of photoionization

Yulin Guo, Yanru Li, Yifei Zhu* and Anbang Sun*

School of Electrical Engineering, Xi'an Jiaotong University, State Key Laboratory of Electrical Insulation and Power Equipment, Xi'an 710049, People's Republic of China

E-mail: yifei.zhu.plasma@gmail.com and anbang.sun@xjtu.edu.cn

Received 19 August 2022, revised 26 December 2022
Accepted for publication 1 February 2023
Published 14 February 2023

Abstract

A diffusive ionization wave can be generated by an ultrafast high voltage far exceeding the inception threshold, and is featured by its unique and repetitive conical morphology. A combinative experimental and numerical study of the diffusive ionization waves is conducted in this work to investigate the role of photoionization in different N_2/O_2 mixtures with oxygen concentrations of 20%, 2%, 0.2%, 1 ppm, and pure nitrogen. In all gas mixtures, the ionization wave first forms a spherical shape after its inception then a conical when it approaches the plane electrode. Compared with typical filamentary streamers and inception cloud generated by low overvoltage, photoionization in a diffusive ionization wave takes effects mainly before the formation of the spherical ionization wave, and affects slightly the propagation velocity, discharge morphology, and the width (diameter) of the ionization wave. When the pin-to-plane electrode gap distance is kept 16 mm, in the atmospheric pressure simulation with an 85 kV voltage pulse, the maximum ionization width decreases from 11.4 mm in the 20% mixture to 9.1 mm in pure nitrogen. In the 200 mbar pressure experiment with a 16 kV voltage pulse, the maximum ionization width decreases from 12.5 mm in the 20% mixture to 11.6 mm in pure nitrogen. E in the inception cloud diameter estimation function ($D = 2\,U\,E^{-1}$) is modified to estimate the width of the ionization wave during its spherical propagation stage. It is shown that the estimation results at 180–205 kV cm^{-1} are in good agreement with the simulation results at atmospheric pressure air.

Keywords: fluid model, ionization wave, photoionization, streamer discharge, plasma modeling

(Some figures may appear in colour only in the online journal)

1. Introduction

The positive diffusive ionization wave, also referred to as the diffuse streamer or spherical streamer [1, 2], is commonly generated in a short pin-to-plane gap under a nanosecond pulse with extreme overvoltage. It is an important way to produce high-energy active species in a large volume, thus it has great potential in the application of plasma-assisted combustion and pollution control. Unlike filamentary streamers generated under low overvoltage, diffusive ionization wave has less randomness and better discharge repeatability during its propagation, and is difficult to branch at atmospheric pressure, which has been studied through several experiments and

* Authors to whom any correspondence should be addressed.

numerical models. Among the limited number of numerical models, the fluid model has been proven a valid method for modeling this kind of discharge by achieving good agreement with experiments in ionization wave velocity, width, and electric field evolution.

Many fluid models are aimed at comparison with experiments. Babaeva and Naidis used an local field approximation (LFA) fluid model to prove that with a higher initial charged species density [3], ionization wave starts to propagate earlier and move with lower velocities, and they explained the polarity effects observed in previous experiments [4, 5]. In addition, they studied the influence of the voltage rise time on the ionization wave characteristics and concluded that the propagation velocity increases with a shorter rise time of the pulsed voltage [6]. Marode *et al* used an LFA fluid model to compare the electron and electric field distributions between 50 kV and 10 kV under the same voltage rise rate, and discussed the generation of runaway electrons (RAEs) during the positive diffusive ionization wave [7]. They concluded that although there may be some RAEs created in the initial stage of the positive discharge, the fluid model is able to describe the discharge process within a certain error range. Tardiveau *et al* also conducted a simulation with a 50 kV amplitude nanosecond pulse and achieved good agreement with their experiment results in discharge morphology, yet the simulated ionization wave propagation velocity is slower [8]. Later, the maximum reduced electric field (*E*/*N*, hereinafter) and ionization wave velocity obtained in simulation by Brisset *et al* agree with their spectral measurement results under an 85 kV pulse [9]. Zhu *et al* conducted a direct comparison between the experiments of Chng *et al* [10, 11] and a local mean energy approximation (LMEA) and an LFA fluid model by using electrodes and applied voltage exactly consistent with those in the experiment [12]. The simulation results not only fit the E-FISH measurement results of the atmospheric diffusive ionization wave in the electric field but also fit the discharge morphology and ionization wave propagation velocity, and showed that the LMEA results fit the electric field evolution measured in the experiment better. Later, Bourdon *et al* disscussed the E-FISH measurement accuracy in diffusive ionization wave combined with the same 2D axisymmetric LFA model in [13], and they pointed out that the E-FISH measurement accuracy is poorer at the intermediate phase when the measurement point is immediately behind the ionization wave front [14].

For it is easier to adjust the parameters (e.g. voltage signals, geometry, and gas components) in the simulation, several researchers also used the fluid model to study the influence of applied voltage and geometry parameters on the diffusive ionization wave. Komuro *et al* explored the effect of the voltage rise rate on the streamer characteristics [15]. Their results show that the streamer characteristics including velocity, electric field strength, and diameter depend on the average applied voltage (defined by the time between the streamer inception and arrival) instead of the voltage rise rate. Their simulated streamer velocities agree well with their experiments [16, 17]. Besides, it is worth noting that they also found that these streamer characteristics are independent of the electrode curvature. This result is later confirmed by the findings of Bourdon *et al* [18]. Bourdon *et al* revealed the electric field evolution of the diffusive ionization wave under a 50 kV pulse with 0.5 ns and 1.5 ns rise time with a LFA fluid model [13] and verified the correctness of their calculated electric field by comparing with the experimental research of Brisset *et al* [9] and Chng *et al* [10]. Later they further studied the influence of electrode geometry on the discharge characteristics with the same model and revealed that the sharpness of the pin electrode has negligible influence on the discharge characteristics and that a disc holder at the end of a pin electrode can effectively suppress parasite radial discharges [18].

For bearing the similarity in discharge morphology, the inception cloud generated by a low overvoltage and the diffusive ionization wave generated by an extreme overvoltage are regarded as similar phenomena [19, 20]. However, their differences in characteristics due to different generation conditions still need further investigation. The inception cloud is a stage between the avalanche and the elongated streamer [19]. It has already been proved that the oxygen concentration in N_2/O_2 mixtures can greatly influence some characteristics (the morphology, propagation velocity, etc) of an inception cloud [20–22], indicating that photoionization plays an important role. The influence of oxygen concentration and photoionization on the filamentary streamers in N_2/O_2 mixtures was also investigated through simulations and experiments: the simulation work of Pancheshnyi *et al* [23] focused on the filamentary streamer characteristics in pure nitrogen and the 1% oxygen concentration gas mixture. Their results show that positive streamer propagates faster and its width is much wider in the case of the 1% mixture in comparison to the case of pure nitrogen when different photoionization functions are considered. Later, the experimental [21, 22, 24,25] and computational [26–28] results on the filamentary streamers of many other researchers drew similar conclusion. As for the diffusive ionization waves, Beloplotov *et al* studied the subnanosecond breakdown process in various gases (air, nitrogen, methane, hydrogen, argon, neon, and helium) and found that the discharge morphology remains diffusive in different gases and that the ionization wave propagates at a velocity of several centimeters per nanosecond and higher [29, 30].

Despite there being some simulation work on the diffusive ionization wave characteristics, most of them have focused on the discharge in atmospheric air, and limited works have discussed it in different gas components [29], especially in N_2/O_2 mixtures. Besides, due to the strong ionization process during its development, the source of seed electrons might change [7], and whether the role of photoionization is still the same as that of filamentary streamers remains unclear. To better understand its physical mechanisms, especially the role of photoionization, and the characteristic differences between it and the classic inception cloud, it is necessary to study the ionization wave characteristics in different oxygen concentrations N_2/O_2 mixtures.

By setting the electrodes and applied voltage of an LMEA fluid model exactly consistent with those in the experiment, the discharge morphology, ionization wave propagation velocity, electric field, and electron density evolution are studied by adjusting the oxygen concentration in the gas mixtures. The structure of this paper is organized as follows: model description and parameter settings are introduced in section 2. The influence of oxygen concentration and photoionization on atmospheric discharge characteristics is discussed in sections 3.1 and 3.2. An experimental and numerical comparison of diffusive ionization wave characteristics at 200 mbar pressure is conducted in section 3.3. Finally, conclusions are given in section 4.

2. Model description

2.1. Coupling equations

The 2D *PASSKEy* (PArallel Streamer Solver with KinEtics) code is used in this paper. The code was used in modeling the nanosecond diffuse discharge at atmospheric pressure and fast ionization wave discharge under moderate pressure [12], and achieved good agreement with the experiments of Brisset *et al* [9] and Chng *et al* [10, 11]. Detailed mathematical methods and model validations can be found in previous publications [12, 31–33].

As pointed out in a previous study [34], the LFA can cause some discrepancies in the electric field, electron-ion density, and streamer velocity with the particle model. Besides, it has been proved that the LMEA provides more accuracy [35, 36] and suits the small grid size simulations better at atmospheric pressures [12]. So in this paper, all the simulations are conducted with LMEA.

In this model, the drift-diffusion equations for species are solved as shown in equation (1), Poisson's equation for the electric field is solved as shown in equation (2), and to calculate the photoionization source term in N_2/O_2 mixtures in a more general way, including pure nitrogen and very low oxygen concentration mixtures, we used the generalized Helmholtz equations in equation (3) through replacing the partial pressure of oxygen molecules p_{O2} with the total pressure p in the classical three-exponential Helmholtz model [37].

$$\frac{\partial n_i}{\partial t} + \nabla \cdot \Gamma_i = S_i + S_{\text{ph}} \tag{1}$$

$$\nabla(\varepsilon_0 \varepsilon_r \nabla \varphi) = -\sum_{i=1}^{N} q_i n_i \tag{2}$$

$$S_{\text{ph}} = \sum_j S_{\text{ph}}^j \tag{3a}$$

$$\nabla^2 S_{\text{ph}}^j(\vec{r}) - (\lambda_j p)^2 S_{\text{ph}}^j(\vec{r}) = -A_j p^2 \frac{p_q}{p+p_q} I(\vec{r}) \tag{3b}$$

$$\frac{\Psi_0(r)}{p} = (pr) \sum_j A_j e^{-\lambda_j pr} \tag{3c}$$

$$\frac{\Psi_0(r)}{p} = \frac{1}{4\pi} \frac{\omega}{\alpha_{\text{eff}}} \frac{\int_{\lambda_{\min}}^{\lambda_{\max}} \xi_\lambda (\mu_\lambda/p) \exp((-\mu_\lambda/p)pr) I_\lambda^0 d\lambda}{\int_{\lambda_{\min}}^{\lambda_{\max}} I_\lambda^0 d\lambda} \tag{3d}$$

In equation (1), n_i is the density of species, S_i is the source term of species, S_{ph} is the photon ionization source term. In equation (2), ε_0 and ε_r are the permittivities of vacuum space and the relative permittivity of air, φ is the electric potential, q_i is the charge for species, and N is the number of charged species.

In equation (3), λ_j and A_j are fitting coefficients for photoionization functions, p is the gas pressure, p_q is the quenching pressure of the excited molecule, $\Psi_0(r)/p$ is the photoionization function that characterizes the photoionization rate. To calculate the photoionization function, α_{eff} is the effective Townsend ionization coefficient, ω is the excitation coefficient of emitting states. The scaling factor $\omega/\alpha_{\text{eff}}$ is taken 0.01 in nitrogen, 0.02 in oxygen, and 1.00 in air, which are based on Pancheshnyi's work [38]. ξ_λ and μ_λ are the spectrally resolved photoionization yield and the absorption coefficient. ξ_λ is calculated through $\sigma_{\text{ionization}}(\lambda)/\sigma_{\text{absrobtion}}(\lambda)$, and μ_λ/p is calculated through $\sigma_{\text{absrobtion}}(\lambda)p/k_B T$. $\sigma_{\text{ionization}}(\lambda)$ and $\sigma_{\text{absrobtion}}(\lambda)$ are photo-absorption and photo-ionization cross-sections at specific wavelengths, which are based on [39]. $I_\lambda{}^0$ is the spectral density of ionizing radiation, which is based on [40, 41]. ($\lambda_{\min}$, $\lambda_{\max}$) is the spectral range of the radiation decided by the threshold ionization energy and the dominating radiation transitions at higher energy levels.

In this work, the photoionization functions Ψ_0/p in different gas mixtures are calculated through the PHOTOPiC toolbox [12, 42], and the six fitting parameters for the generalized extended three-exponential Helmholtz equation are fitted based on the Nelder–Mead simplex direct search method. The Ψ_0/p calculation comparison with Zheleznyak's model [43] and Pancheshnyi's results [38] are compared. It has to be noted that Janalizadeh and Pasko [44]. Proposed a general framework for photoionization in air theoretically, where the contributions of each band system of N_2 to photoionize O_2 in air are calculated. Their model produces a similar photoionization function to the model of Zheleznyak *et al* [43]. Figure 1(a) shows the calculated Ψ_0/p in air, and the experiment results are extracted from [45]. Figure 1(b) shows the calculated Ψ_0/p in different N_2/O_2 mixtures, and the experiment results are extracted from [46]. It also shows the Ψ_0/p on ionizing the oxygen and nitrogen molecules in the 1 ppm mixture (see the solid dark blue line and the solid orange line), showing that in such low oxygen concentration gas mixtures ionizing N_2 molecules becomes the main process of photoionization, and that the main sources of photons are from the by dissociative ionization (see equation (4) [38]). The six fitting λ_j and A_j coefficients in different gas mixtures are given in table 1.

$$N_2 + e \rightarrow N^+(^1P^0, {}^3P^0) + N + 2e \tag{4a}$$

$$N^+(^1P^0, {}^3P^0) \rightarrow N^+(^3P) + 67.1\text{nm} \tag{4b}$$

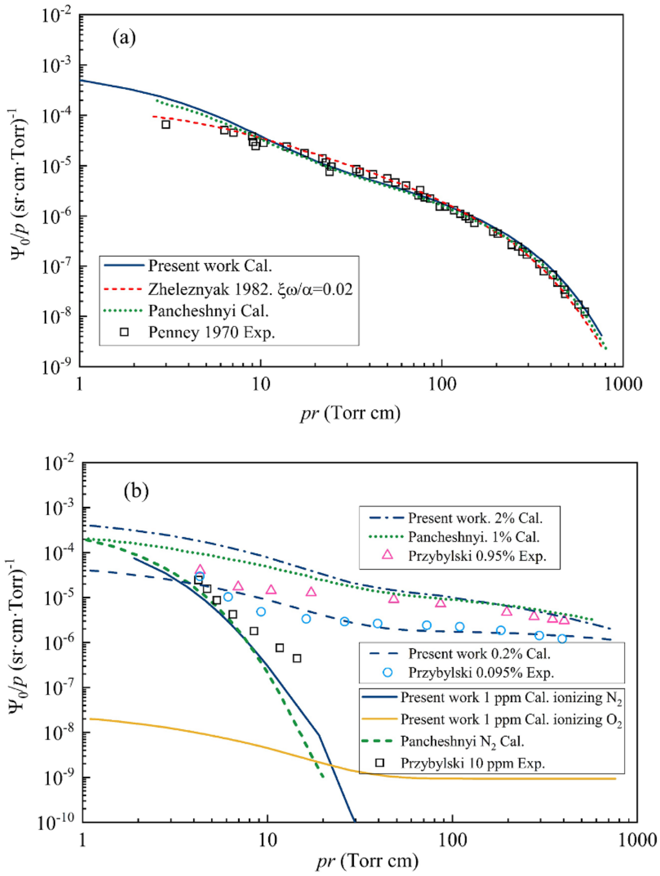

Figure 1. (a). The comparison between calculated and measured pressure-reduced photoionization function in air. Pancehshnyi's calculation result is extracted from [38]. The experiment result is extracted from [45]. (b). The comparison between calculated and measured pressure-reduced photoionization function in different N_2/O_2 mixtures. Pancehshnyi's calculation results are extracted from [38]. The experiment result is extracted from [46].

Table 1. Fitting parameters in different gas mixtures.

Parameters	Pure nitrogen	N_2 with 1 ppm O_2	N_2 with 0.2% O_2	N_2 with 2% O_2	N_2 with 20% O_2
A_1 (cm^{-2} $Torr^{-2}$)	6.646×10^{-2}	1.808×10^{-1}	1.220×10^{-4}	1.190×10^{-3}	1.207×10^{-3}
A_2	1.3580	4.535×10^{-1}	5.039×10^{-7}	2.664×10^{-6}	1.301×10^{-6}
A_3	−1.4165	-6.334×10^{-1}	1.876×10^{-5}	1.634×10^{-4}	3.928×10^{-4}
λ_1 (cm^{-1} $Torr^{-1}$)	1.3121	1.4077	1.516	1.452	1.419
λ_2	1.5238	1.4480	0.487×10^{-1}	0.401×10^{-1}	4.093×10^{-2}
λ_3	1.5097	1.4359	3.637×10^{-1}	3.420×10^{-1}	4.855×10^{-1}

The discharge energy release and gas temperature are calculated by solving Euler equations. The calculated density and temperature are further used for calculating the reduced electric field. The detailed coupling methods can be seen in [32].

2.2. Simulation set-up

The boundary conditions, approximations, and application ranges of this model are detailed described in [12], and will not be detailed in this paper again. In this model, 15 species and 34 reactions in N_2/O_2 mixtures are considered [32], in which the kinetics scheme describing the streamer propagation [47] and fast gas heating are [48] combined. The detailed reactions are shown in table A1 in appendix A.

10^{10} m^{-3} background electrons and ions are set uniformly in the computation domain, similar values can be found in both PIC/MCC model [27] and fluid model [13]. The pin-to-plane electrode geometry is shown in figure 2(a), which is the same as the E-FISH experiment in [10]. The curvature radius of the pin electrode is 50 μm, the radius of the plane electrode is 50 mm, and the gap distance between them is 16 mm. It is worth noting that there is a 'disc holder' at the end of the pin electrode. Figure 2(b) shows the applied over-voltage nanosecond pulse which can generate field ten times the stability field for positive ionization waves in ambient air. The applied voltage pulse starts from 5 kV at 0 ns, and reaches the peak at 2.8 ns, with an average voltage rise rate of 28.5 kV ns^{-1}.

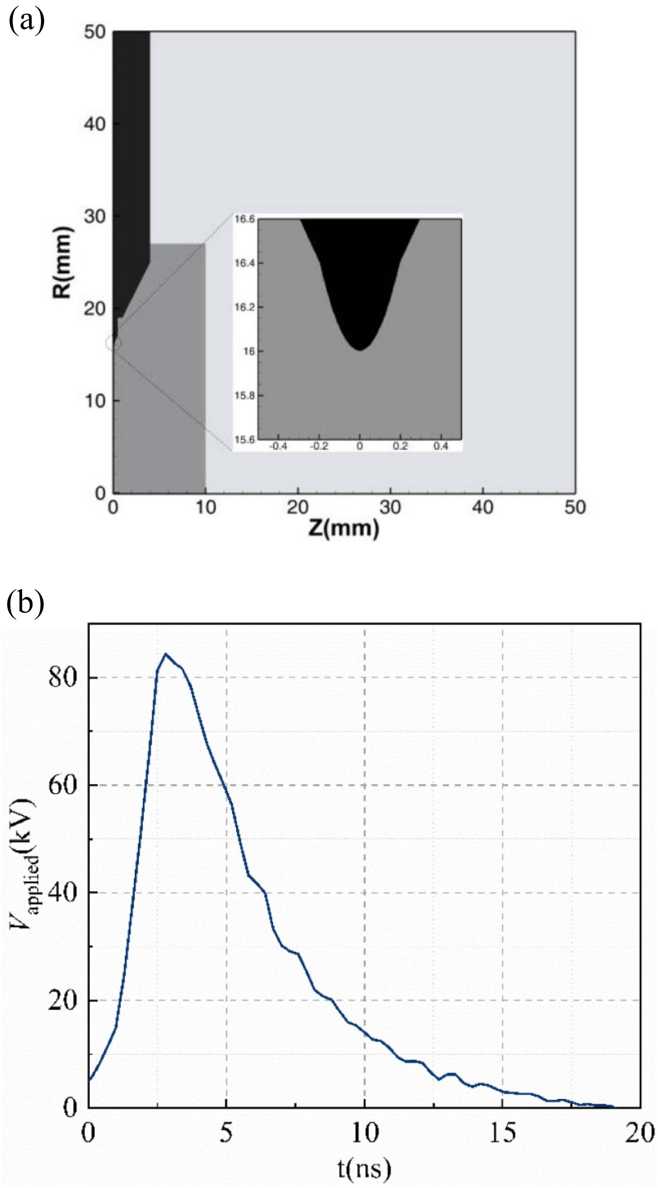

Figure 2. (a). The 50 mm × 50 mm computational domain in the simulation. Poisson's equation and Helmholtz equation are solved in the entire domain. Drift-diffusion equations are solved in the dark grey domain. Euler equations are solved in the light and dark grey domain. (b). The applied voltage in the simulation.

3. Results and discussion

3.1. Discharge characteristics in different oxygen concentration N_2/O_2 mixtures at atmospheric pressure and its comparison with the inception cloud

By setting the oxygen concentration as 20%, 2%, 0.2%, 1 ppm, and completely with no oxygen in the N_2/O_2 mixtures, the discharge characteristics and the effect of photoionization in diffusive ionization waves are discussed in this section.

Figures 3 and 4 show the discharge propagation process is similar in different gas mixtures: first propagates in a spherical shape until the ionization wave head is enhanced and forms a conical shape. Here we take the discharge in the 20% mixture (see figures 3(a) and (b)) for example to introduce this process. After the ignition of the discharge, the ionization wave propagates with a spherical shape (from t = 1.5 ns to t = 2.5 ns). At 2.5 ns, the ionization wave head propagates nearly half the gap. E/N of the ionization wave head is enhanced by the space charge and the plane electrode, then it accelerates and forms a protrusion at the bottom of the sphere. Eventually, the ionization wave forms a conical shape at 3.1 ns and connects to the plane electrode. During its propagation, the reduced electric field E/N of the ionization wave head first decreases then starts to increase after 2.5 ns. E/N reaches its maximum of 1330 Td at the moment before the steamer connects the plane electrode at 3.1 ns. However, this high E/N value lasted less than 0.2 ns and then decreased to an average value of about 200 Td due to the formation of the discharge channel. After that, E/N in the channel changes with the Laplacian field. This whole development process is considered to be similar to that of the filamentary streamers, the spherical shape after the discharge ignition bears similarity in morphology with the inception cloud. After that, the formation of the protrusion and the conical shape corresponds to the break of the inception cloud and the elongated filamentary streamer, which also accelerates when approaching the plane electrode.

Note that 'side flares' (parasite streamers) appeared above the main ionization body at the position where the radius of curvature of the electrode changes significantly. Bourdon *et al* showed that a 'disc holder' at the end of the electrode or a smoother-shaped electrode can effectively suppress the parasite streamers in their work [18]. We tested a rod-shaped electrode with a disc holder in our model with the 85 kV amplitude voltage, though no obvious streamers are observed, the electron density exceeds 10^{19} m^{-3} and E/N exceeds 300 Td near the cylindrical area of the electrode. Thus in this work, we still choose to use an electrode shape consistent with the experiment. It is also worth noting that in the experimental work of Brisset *et al* [9] and Pechereau *et al* [49], obvious side flares were observed.

Figures 3 and 4 also show that with the decrease of oxygen ratio in the gas mixture, the diffusive ionization wave morphology remains, but the width of both side flares and ionization wave body shrinks. The maximum ionization wave width is determined by the 10^{18} m^{-3} electron density isoline. It decreases from 11.4 mm in the 20% mixture to 9.1 mm in pure nitrogen, and the maximum width appears at about $Z = 9$ mm. The maximum width of the ionization wave body changes only slightly in different gas mixtures is similar to the experimental results of Beloplotov *et al* [29]: In their experiment, the positive diffusive ionization wave width almost remains unchanged in air, nitrogen, and argon (3 mm gap and a 40 kV voltage amplitude). However, compared to the shrink of the inception cloud or filamentary streamers in air and pure nitrogen generated by low overvoltage pulses, the decrease in diffusive ionization wave width can be considered to be very limited: as shown in figure 1, the photoionization function used is reduced by 20 to over 10^3 times from 20% mixture to nitrogen at 10–100 cm·torr, but the maximum ionization wave width at atmospheric pressure only decreases by 20%. Thus it can be concluded that the diffuse discharge morphology is mainly

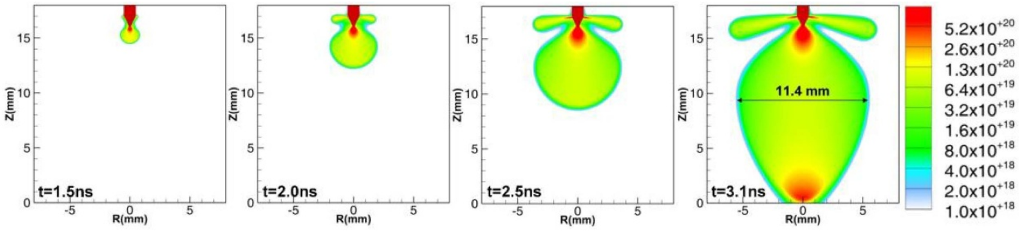

(a)the electron density evolution in the 20% mixture at 1 atm

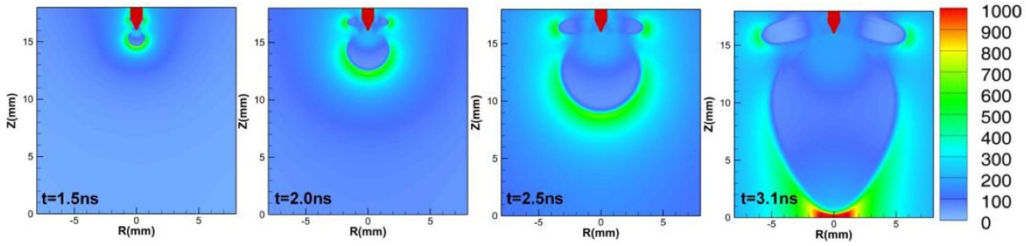

(b)the electric field evolution in the 20% mixture at 1 atm

Figure 3. The electron density and reduced electric field evolution in the 20% mixture. The electron density is in m^{-3}, and *E*/*N* is in Td. Note that the model in 20% mixture is the same as the model in [12].

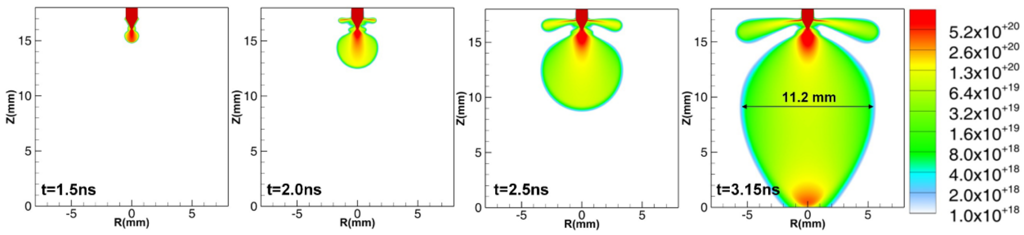

(a) the electron density evolution in the 0.2% mixture at 1 atm

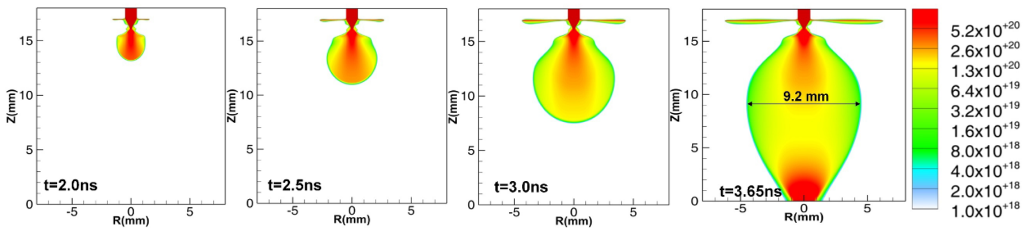

(b) the electron density evolution in the 1 ppm mixture at 1 atm

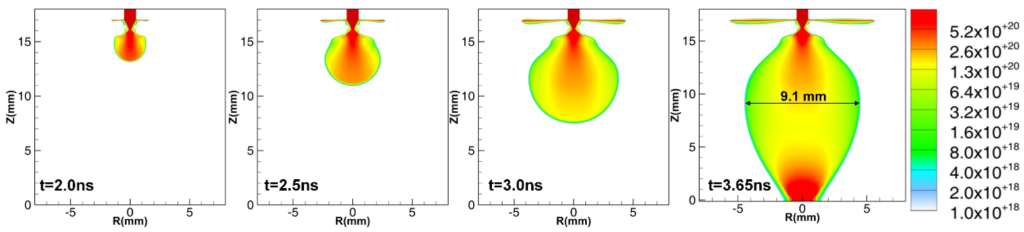

(c) the electron density evolution in pure nitrogen at 1 atm

Figure 4. The electron density evolution in different mixtures. The electron density is in m^{-3}.

determined by its extreme overvoltage and the direct ionization process. The discharge ignites under a high voltage with a fast overvoltage applied, so the effective ionization coefficient remains a high value in a rather large volume due to its high Laplacian field, resulting in the rapid increase of the ionization wave width and velocity.

It is also worth noting that the discharge process and morphology are more similar in the 1 ppm mixture and

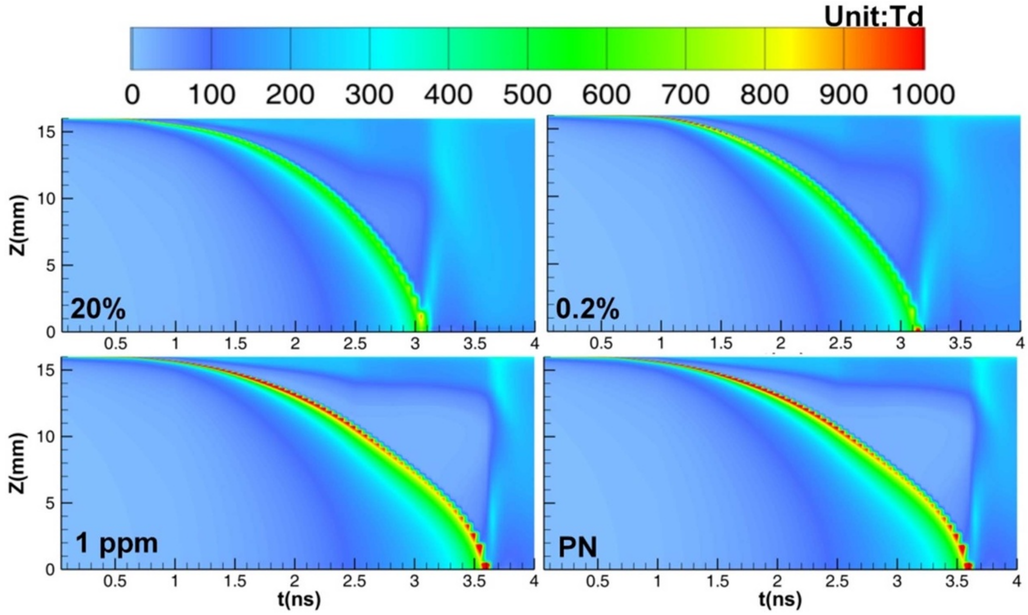

Figure 5. The steak image of axis E/N evolution in different mixtures at 1 atm. PN stands for pure nitrogen.

pure nitrogen compared to other mixtures, showing that the reactions and photoionization of oxygen no longer dominate in the 1 ppm mixture as mentioned in section 2. The electron density inside the streamer channel in pure nitrogen is higher than in other mixtures, and the electron density exceeds 10^{21} m^{-3} in the vicinity of the pin electrode.

Figure 5 shows the time dependence of E/N on the symmetry axis ($r = 0$ mm). The horizontal axis in each figure is the discharge time (0–4 ns), and the vertical axis is the discharge gap (0–16 mm). The color in the figure shows the strength of E/N on the axis. It is strongest at the head of the ionization wave, so the streak in each figure shows the trajectory of ionization wave heads during its propagation. It shows that the ionization wave ignites and reaches the plane electrode slower with the decrease of oxygen concentration: The ignition time delays from 0.5 ns in the 20% mixture to 0.6 ns in pure nitrogen, and the ionization wave reaches the plane electrode at 3.1 ns in the 20% mixture, 3.15 ns in 0.2%, 3.55 ns in 1 ppm, and 3.6 ns in pure nitrogen. However, during the ionization wave propagation, E/N at its head increases with the decreasing oxygen concentration, and remains higher than 800 Td during propagation in pure nitrogen. This is because the effective ionization coefficient in pure nitrogen is higher than in other oxygen-containing electronegative gases due to the lack of electron attachment, and results in a stronger ionization process, leaving a higher density of electrons and positive ions at the ionization wave head (see figure 4(c)), thus the space charge field increases. Filamentary streamers also show a similar characteristic [23].

For a more detailed comparison between E/N in various gases, E/N at $Z = 13$ mm is extracted and shown in figure 6. The 20% mixture line has already been proven to agree with

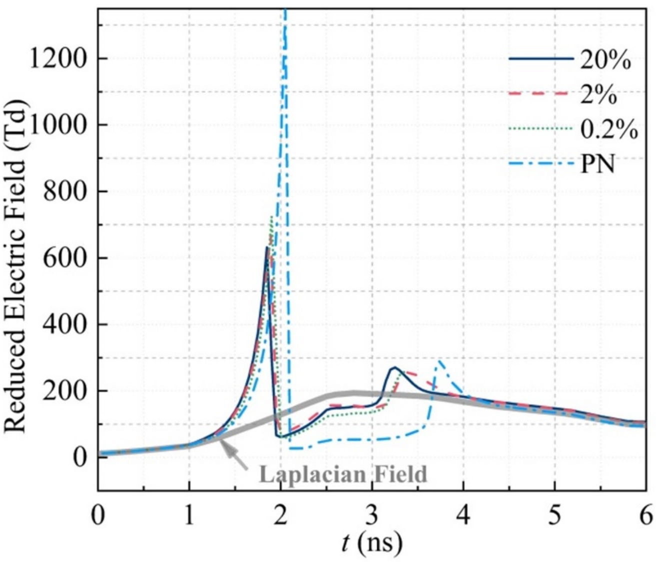

Figure 6. E/N evolution at $Z = 13$ mm in different mixtures. PN stands for pure nitrogen.

the experiment results of E-FISH measurements [12]. The first peak corresponds to the ionization wave head reaching the $Z = 13$ mm point, after that a rapid decrease in E/N shows up due to the self-shielding effect inside the ionization wave body. Then E/N slowly increases again as the discharge propagates and the Laplacian field rises. After it connects two electrodes, a return stroke shows up and results in the second peak of E/N near the pin. After this stroke, E/N changes with the Laplacian field due to the connection.

The evolution of E/N at $Z = 13$ mm also varies greatly in different gas mixtures. The first peak decreases with the

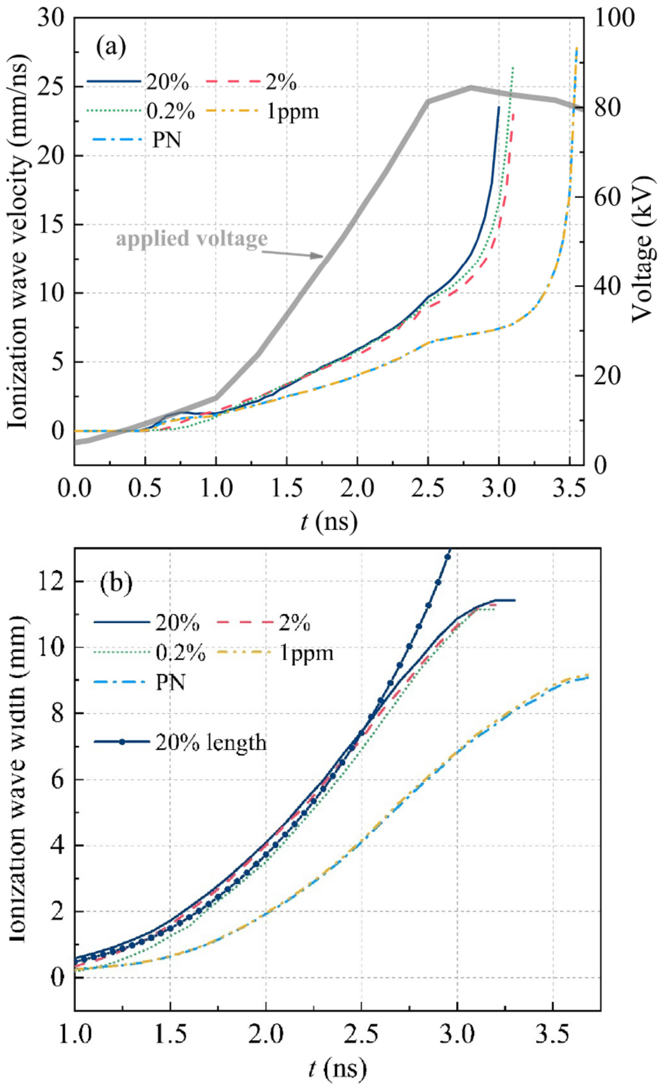

Figure 7. The diffusive ionization wave velocity and width in different mixtures at 1 atm. PN stands for pure nitrogen. The dark blue solid line with dots in (b) is the length of the ionization wave in the 20% mixture during its propagation.

decreasing oxygen ratio, and it reaches as high as 1350 Td in pure nitrogen. Yet due to the late ignition and slow propagation velocity, it reaches $Z = 13$ mm in pure nitrogen later. Huge electric field differences in different gas mixtures were also found in the filamentary streamer by a 3D Particle-in-Cell/Monte Carlo Collision (PIC-MCC) model [27], in which the electric field in the 0.2% mixture is higher than that in the 20% mixture. E/N under the self-shielding effect (between the first and second peak) also decreases with the decreasing oxygen ratio, reaching the lowest 25 Td at 2.15 ns in pure nitrogen.

The ionization wave propagation velocity and its maximum width in various gases are shown in figure 7. The velocity data is cut before the discharge connection and calculated according to the maximum E/N at its head. The maximum width is cut after the connection and calculated according to the 10^{18} m^{-3} electron density isoline. A similar characteristic calculation method can also be found in [13].

Figure 7(a) shows two clear stages during the discharge acceleration process: a linear acceleration stage and an approximate exponential acceleration stage. As mentioned before, the linear acceleration stage corresponds to the spherical shape propagation process and ends at 2.5 ns. The solid line with dots in figure 7(b) shows the length of the ionization wave in the 20% mixture during its propagation, comparing it to its width, it shows that from 1.0 ns to 2.55 ns, it propagates in its spherical stage. After that, the ionization wave is elongated longitudinally.

The average velocity decreases with the decreasing oxygen ratio, ranging from 6.5 mm ns^{-1} in the 20% mixture to 4.5 mm ns^{-1} in pure nitrogen, which is higher than the classic 3.5 mm ns^{-1} measured in [50] (40 mm gap, 80 kV, 15 ns rise time, 1 atm air). Streamer velocities can be influenced by various factors: applied voltage, photoionization, background ionization, etc. The streamer velocities in different gas mixtures were also reported quite differently: for filamentary streamers, it is reported that the velocity in nitrogen is lower than in air at 1 bar, but the velocity is higher in nitrogen at a lower pressure [20, 22]. However, the streamer in pure

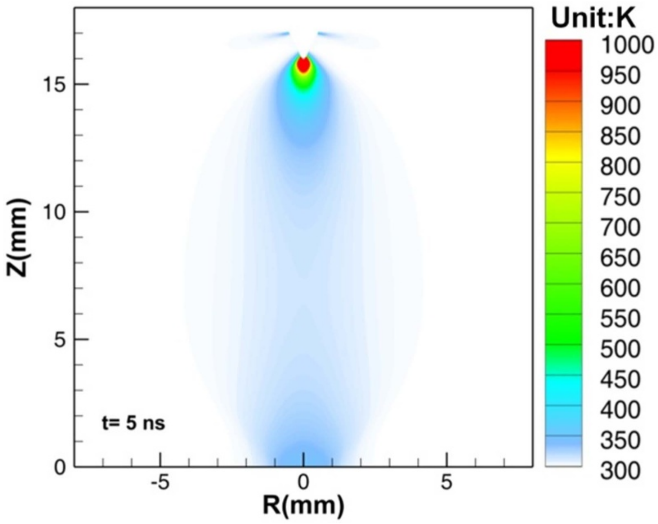

Figure 8. The gas temperature distribution after the discharge connects the plane electrode in the 20% mixture at 1 atm.

nitrogen propagates faster in the simulation of [23], but slower in [26].

Figure 7(b) also shows the maximum ionization wave width also decreases with the decreasing oxygen concentration, it decreases by 20% (from 11.4 mm to 9.1 mm) in pure nitrogen compared to the 20% mixture. While the diameter of the inception cloud decreases more in pure nitrogen, for example, it decreases by 84% from 55 mm in 20% mixture to 9 mm in 'pure nitrogen' in our experiment (see figures 18(d) and (e)).

The maximal diameter of the inception cloud in air can be estimated through the following equation (5) [19], where U is the voltage applied to the electrode and E_k is the breakdown field at the head of inception cloud. In the 20% mixture, take $E_k = 32$ kV cm^{-1} and the $U = 33$ kV at $t = 1.5$ ns when the ionization wave is still spherical. The calculated diameter $D = 2$ cm. However, the actual maximal width in both simulation and experiment is far less than this value, and this is because the electric field at the ionization wave boundary is much bigger than E_k, the typical electric field strength at the edge of the inception cloud. In the next section, we manage to modify this estimation equation by replacing the boundary electric field.

$$D = 2R_{\mathrm{max}} = 2U/E_k \tag{5}$$

The total energy deposition during the discharge process in 20% mixture is calculated according to equation (6), in which $\boldsymbol{j}_i$ is the specie flux, Ω is the whole plasma region, and m is the number of species ($m = 15$ in our simulation). The calculated deposited energy is 83.9 mJ, which is slightly lower than the 100 mJ result of Tardiveau *et al* [8] (80 kV amplitude, 16 mm gap). The gas temperature after the discharge connects the plane electrode (at 5 ns) in the 20% mixture is shown in figure 8. The gas temperature in the vicinity of the pin electrode (from $Z = 15.5$ mm to 16 mm) exceeds 1200 K, and it is only 420 K at $Z = 14.5$ mm, similar to the 400 K experiment result in [9] (85 kV amplitude, 18 mm gap, also measured at 1.5 mm from the pin). However, for the filamentary streamers like the experiment results of Komuro *et al* [51] (13 mm gap, 24 kV amplitude, 0.52 kV ns^{-1} rising edge, 1 atm pressure, 25 electrodes discharge), it can be calculated that the energy deposition is ∼11.7 mJ, and the results of Li *et al* [52] (160 mm gap, 6.6 kV amplitude, 500 ns pulse length, 100 mbar pressure) is only 0.14 mJ, which is far less than that of the diffusive ionization waves.

$$Q_{\mathrm{Total}} = \sum_i^m \int_\Omega \int_0^t e\boldsymbol{j}_i \cdot \boldsymbol{E}\,\mathrm{d}t\,\mathrm{d}\Omega \tag{6}$$

The similar characteristics between diffusive ionization wave and inception cloud in discharge morphology and propagation mode, as well as their differences in size, velocity, energy deposition, and influence by oxygen concentration, indicate that they need further discussion and comparison.

3.2. Discussion on the role of direct ionization and photoionization during the discharge propagation

As described in the above section, there are two stages during the discharge propagation according to the discharge morphology: the spherical and conical propagation stages. In this section, the different roles of direct ionization and photoionization during the two propagation stages are discussed.

Figure 9 shows the photoionization rate S_{ph} and the ratio of direct ionization rate and photoionization rate $S_{\mathrm{ion}}/S_{\mathrm{ph}}$ at t = 2.5 ns and $t = 3.0$ ns in the 20% mixture. At $t = 2.5$ ns, the spherical propagation stage, $S_{\mathrm{ion}}/S_{\mathrm{ph}}$ remains ∼300 at the spherical shell-like ionization wave head, proving the important role played by the direct ionization in forming the spherical ionization wave head, especially at the places where S_{ph} is lower than 10^{28} m^{-3}s^{-1} ($Z = 10$–14 mm). As for the conical propagation stage at $t = 3.0$ ns, $S_{\mathrm{ion}}/S_{\mathrm{ph}}$ at the ionization wave head became larger and remains ∼600, showing that direct ionization is more pronounced during this stage and reaches

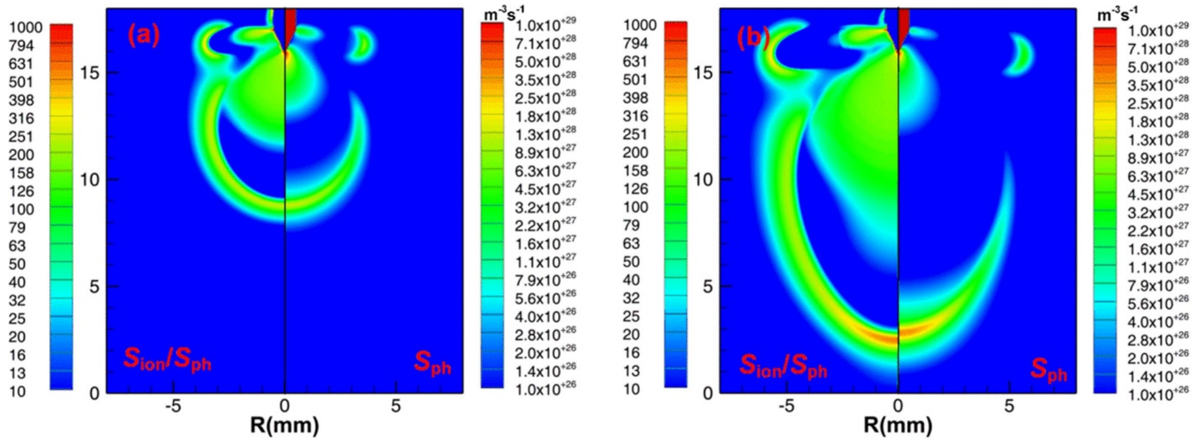

Figure 9. The ratio of direct ionization rate and photoionization rate $S_{\mathrm{ion}}/S_{\mathrm{ph}}$ and the photoionization rate S_{ph}(unit: $\mathrm{m^{-3}s^{-1}}$) at $t = 2.5$ ns and $t = 3.0$ ns in the 20% mixture. (a) $t = 2.5$ ns, (b) $t = 3.0$ ns.

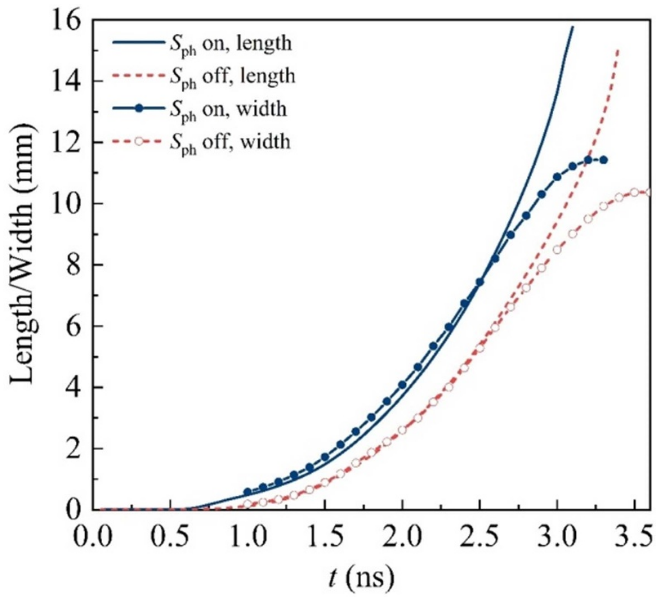

Figure 10. The ionization wave length and width during its propagation in the 20% mixture. 'S_{ph} off' means turning off the Helmholtz equation. The background ionization level in both cases remains 10^{10} $\mathrm{m^{-3}}$.

10^{31} $\mathrm{m^{-3}s^{-1}}$, which is one order of magnitude larger than it in filamentary streamers [23].

To further investigate the role of photoionization, here we turn off the Helmholtz equation, and the results are shown in figure 10. Without photoionization, the ionization wave reaches the plane electrode later, and its maximum width also decreases by about 9%. However, from 1.0 ns to 2.7 ns, the ionization wave maintains its spherical shape even without photoionization, and its maximum propagation velocity also reaches $\sim$25 mm $\mathrm{ns^{-1}}$ when reaching the plane electrode, also proving the importance of direct ionization in the two propagation stages. The role of photoionization can be regarded as providing seed electrons at the initial stage of the ionization wave so that it can propagate faster before the formation of the spherical stage, which is the period from 0 ns to 1 ns in figure 10.

On the other hand, as mentioned in section 3.1, the breakdown field ($E_k = 32$ kV $\mathrm{cm^{-1}}$) is not a proper electric field in estimating the maximum diffusive ionization wave width through equation (5). Here we replace the breakdown field E_k in equation (5) with $E_\mathrm{r} = 205$ kV $\mathrm{cm^{-1}}$ and 180 kV $\mathrm{cm^{-1}}$, which are given by the E-FISH measurement and our calculation result respectively, to estimate the theoretical maximum width (diameter) of the diffuse ionization wave during its spherical propagation phase. The estimated results and the calculated results are shown in figure 11. The estimated maximum ionization wave width is close to the simulated values. Figure 11 also demonstrates the estimated maximum width in pure nitrogen, and $E_\mathrm{r} = 367$ kV $\mathrm{cm^{-1}}$ is the average electric field at the ionization wave head during its spherical propagation phase.

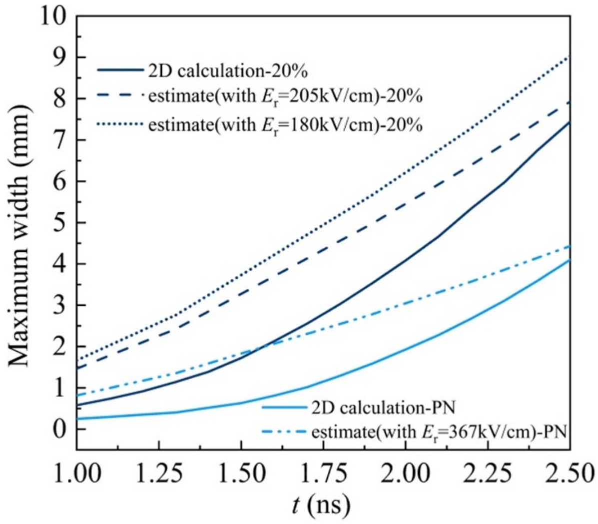

Figure 11. The estimated and calculated maximum ionization wave width during its spherical propagation stage. The solid lines are extracted from the above 2D calculation in section 3.1. The dashed and dotted lines correspond to the estimated maximum width through improving equation (5).

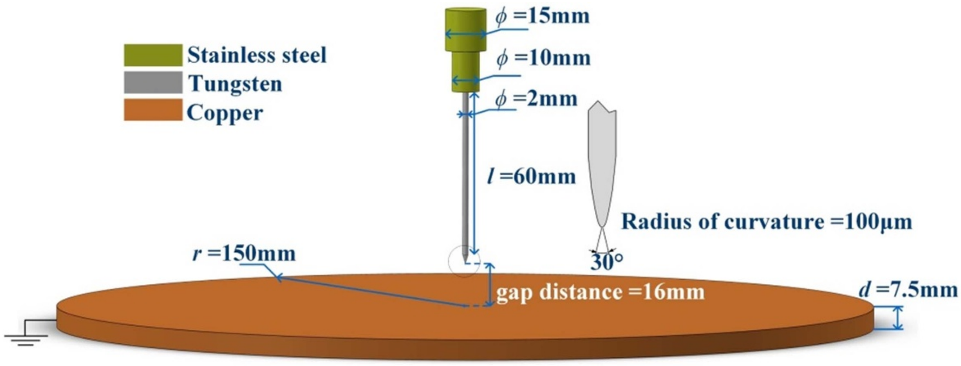

Figure 12. The electrode set-up in the experiment. The curvature radius of the pin electrode is 100 μm, and the gap distance is 16 mm. The radius of the grounded plane electrode is 150 mm.

3.3. Experimental results of the diffusive ionization wave in different oxygen concentration N2/O2 mixtures at 200 mbar pressure

The experiment of diffusive ionization waves in different N_2/O_2 mixtures is conducted in this section to further verify the role of photoionization.

An 85 kV amplitude voltage pulse is difficult to achieve in our experiment, thus the gas pressure is scaled to 200 mbar and the electrode gap distance is set at 16 mm to adapt to the experimental voltage source (16 kV amplitude). The electrode set-up in the experiment is shown in figure 12. There is also a disc holder (colored green) at the end of the pin electrode. The discharge chamber is pumped to less than 5×10^{-5} Pa before each experiment to ensure the purity of the gases.

The applied voltage and the discharge current profiles for the discharge in the 20% mixture are shown in figure 13. The voltage pulse is generated by a nanosecond pulse generator (FID power supply, Model: FPG 50–50NX2), the rise time is 10 ns and its peak value is 16 kV. The discharge ignites at t_0 and reaches the plane electrode at t_c = 5 ns (see the purple region). The discharge morphology images corresponding to the voltage and current profiles are shown in figure 14 (shot with an Andor iStar DH334T intensified CCD camera). It has a similar discharge morphology to the atmospheric discharge in section 3.1: it ignites and propagates with a spherical shape

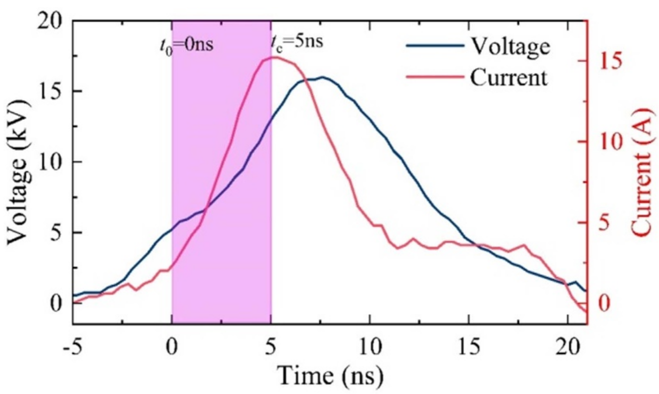

Figure 13. The applied voltage and discharge current profiles. The gas contains 80% nitrogen and 20% oxygen and its pressure is 200 mbar.

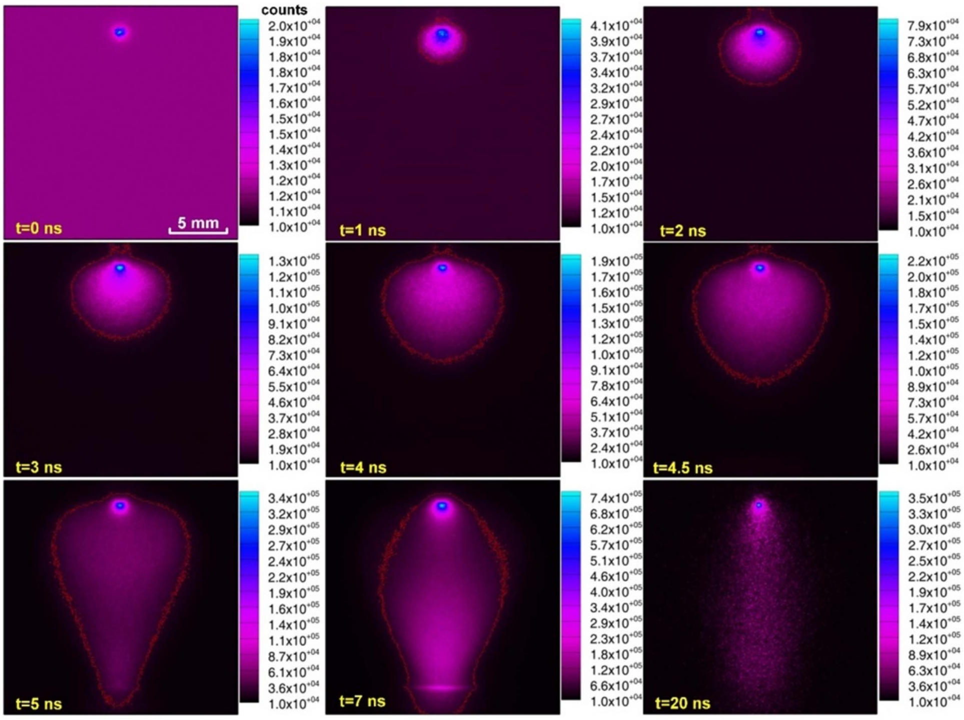

Figure 14. The discharge morphology. Each image is accumulated by 20 discharges. The color legend on the right of each image shows the counts that represent the relative light emission intensity. The gas contains 80% nitrogen and 20% oxygen. The gas pressure is 200 mbar.

(0 ns–3 ns) until its head approaches the plane electrode and a protrusion is produced from its head, then the ionization wave accelerates and reaches the plane electrode (4 ns–5 ns). After the connection (5 ns), the light intensity at the pin and plane electrode increases but the discharge channel shrinks. After 20 ns, the discharge gradually extinguishes, and the light intensity in the channel becomes weaker. The whole discharge process is the same as the process in the atmospheric diffusive ionization wave in [9] (85 kV amplitude, 18 mm gap).

Similar to the simulated results in section 3.1, when the gas components are switched to the 2% mixture, 0.2% mixture, or 'pure nitrogen' (contains ∼10 ppm oxygen), the discharge morphology and length do not change obviously. To investigate the relationship between the discharge characteristics and the gas components, the way of calculating the streamer width and length in [53] is also introduced in this paper as shown in figure 15. To decide the left/right boundary and the ionization wave head of the discharge, I_R and I_Z are calculated through equation (7). The width and length are decided by 15% of the maximum values of I_R and I_Z.

$$I_R(R) = \int_{0\mathrm{mm}}^{16\mathrm{mm}} I(R,Z)dR \qquad (7a)$$

$$I_R(Z) = \int_{-10\mathrm{mm}}^{10\mathrm{mm}} I(R,Z)dZ \qquad (7b)$$

The ionization wave width and length in different gas mixtures are shown in figure 16. The ionization wave width gradually increases until it reaches the plane electrode (∼5 ns in the 20% mixture, ∼5.5 ns in the 0.2% mixture, and ∼6 ns in the 'pure nitrogen', and it should be noted that due to the limitation of the maximum intensified CCD (ICCD) gate width, the accuracy of this connection measurement is within 0.5 ns), after that the maximum width gradually decreases. The propagation process shows a clear acceleration process in figure 16(b). Similar to the results in section 3.1, with the decreasing oxygen concentration, the ionization wave width shrinks and propagates slower, but the maximum width only decreases about 7% from 12.5 mm in the 20% mixture to 11.6 mm in 'pure nitrogen' (decreases 20% from 11.4 mm to 9.1 mm in the calculation in section 3.1), indicating that the influence of the photoionization on it is very limited as discussed above in the simulation.

By modifying the shape of the electrode and the gas pressure in section 2, the discharge at 200 mbar is also simulated. The simulation set-up is shown in figure 17, and the applied voltage is completely the same as that used in the experiment (starting from 5.2 kV).

The simulated diffusive ionization wave characteristics are also shown in figure 16 (see the solid lines). The geometry and voltage profile are the same as those in the experiments. The ionization wave length and width are determined through the maximum E/N at its head and 10^{18} m^{-3} electron density isoline, which is the same as in section 3.1. The comparison shows a good agreement except for the connection time in 'pure nitrogen'. The reason for this connection time difference is still unclear. In our experiment, to limit the influence of possible memory effects on the discharge characteristics from one pulse to another, the voltage pulse frequency is set at 0.2 Hz. For comparison, the discharge frequency in the experimental work of Brisset *et al* [9] is

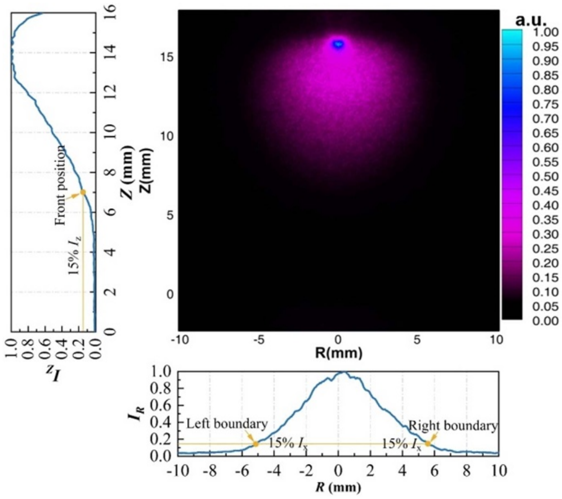

Figure 15. Schematic diagram showing the calculation of the diffusive ionization wave length and width. $Z = 0$ is the position of the plane electrode, and $Z = 16$ mm is the position of the pin electrode.

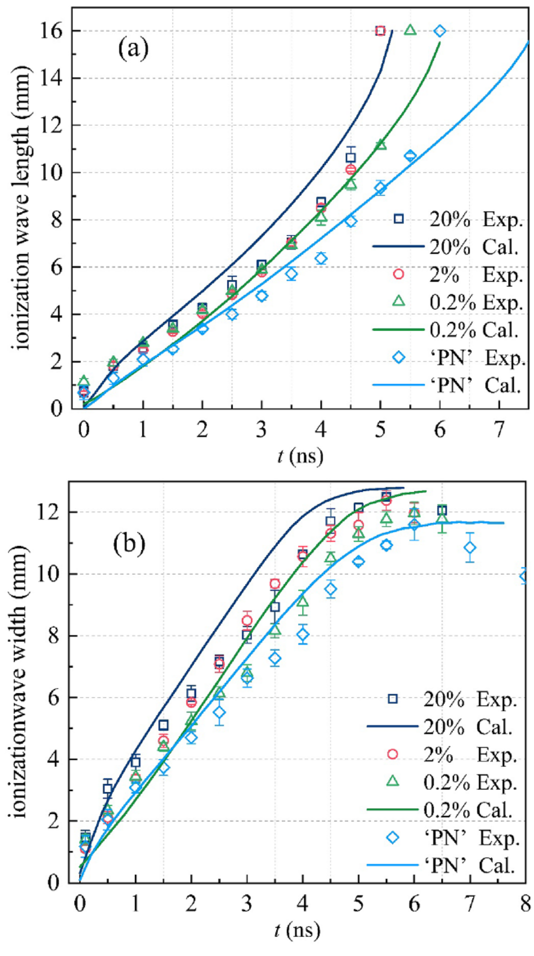

Figure 16. The diffusive ionization wave width (a) and length (b) during the discharge in different gas mixtures at 200 mbar pressure. Each data point is calculated from 10 discharge images. The solid lines show the calculated results.

5 Hz. However, the electron density decrease in low-pressure nitrogen can get much slower and leads to a higher background density for the next discharge. But this effect was not considered in our simulation. This may be one of the reasons causing the time difference (1.5 ns) between simulation and experiment. The calculated $N_2(C^3\Pi_u)$ density distribution during the ionization wave propagation process is shown in figure 18.

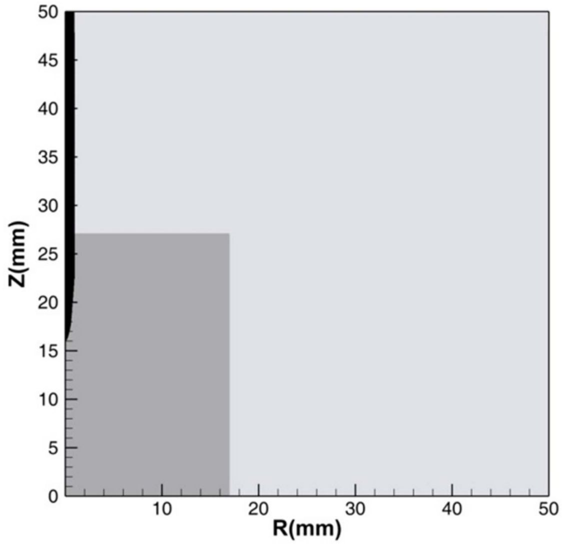

Figure 17. The 50 mm $\times$ 50 mm computational domain in the 200 mbar simulation. Poisson's equation and Helmholtz equation are solved in the entire domain. Drift-diffusion equations are solved in the dark grey domain. Euler equations are solved in the light and dark grey domain.

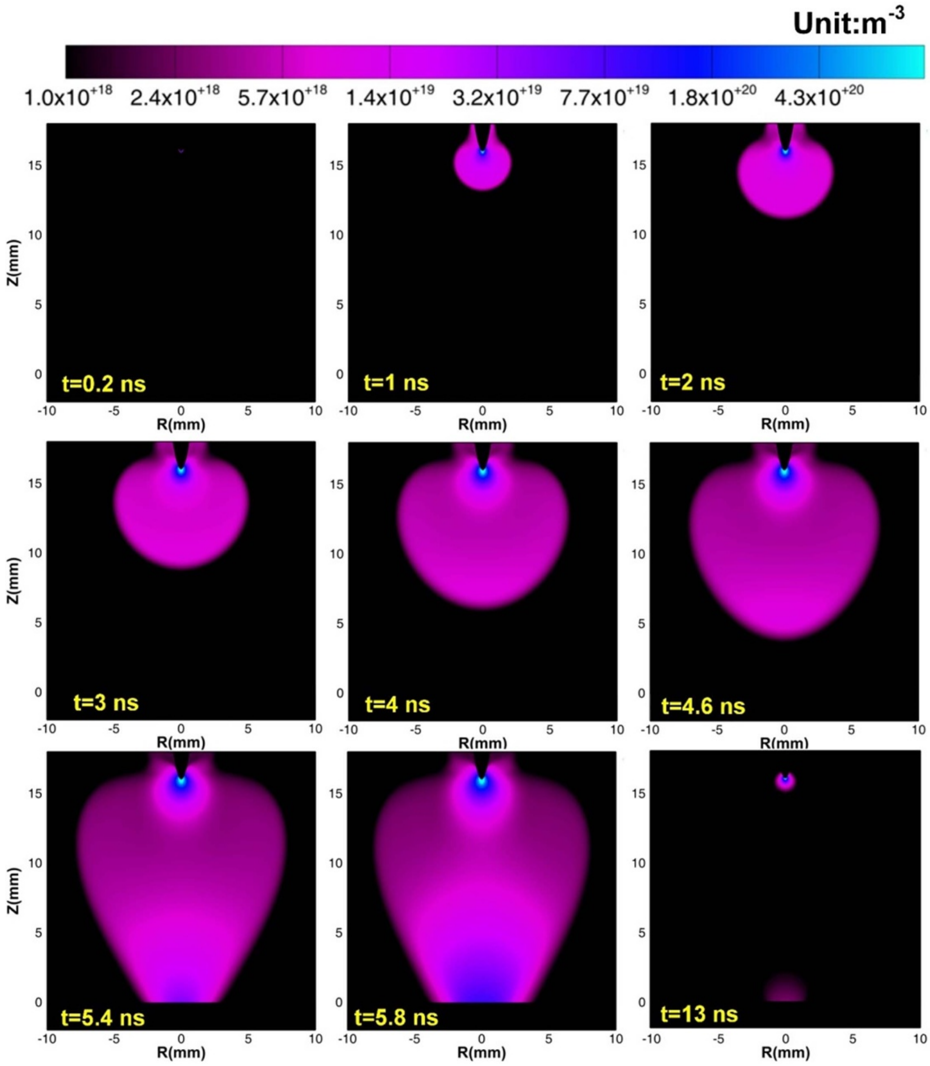

Figure 18. The calculated $N_2(C^3\Pi_u)$ density distribution during the ionization wave propagation.

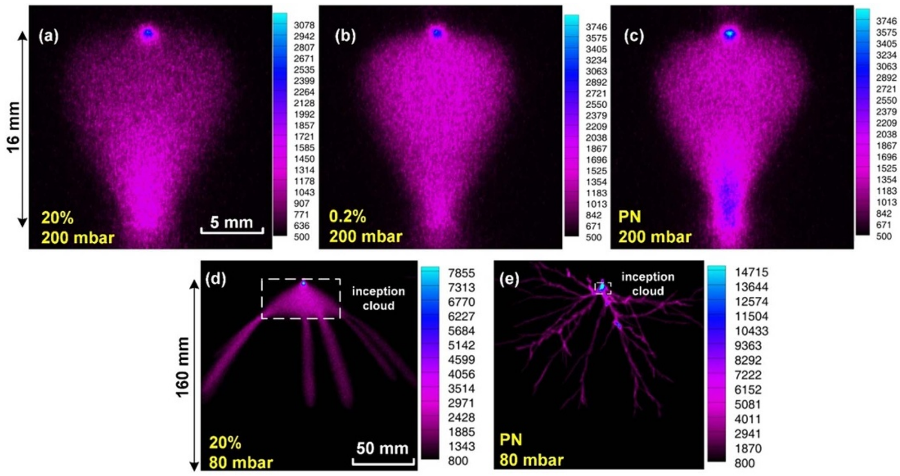

Figure 19. The morphology of the diffusive ionization wave and inception cloud in the mixtures. (a)–(c) are the ionization wave, the gap distance is 16 mm and the ICCD gate width is 2 ns. (d) and (e) shows the classic morphology of the inception cloud, the gap distance is 160 mm and the ICCD gate width is 500 ns. The applied voltage in (d) and (e) is a 12 kV pulse with a 75 ns rising edge and 400 ns duration generated by a solid state switch (Behlke, HTS 901–10-GSM). PN stands for 'pure nitrogen'.

Figure 19 demonstrates the morphology of the diffusive ionization wave and inception cloud in different gas mixtures. Figures 19(d) and (e) show the classic breakup of the inception cloud and the formation of branched filamentary streamers in a 160 mm gap. Despite our 2D fluid model has proven the role of photoionization in section 3.1, it can not simulate the breakup and branching process induced by stochastic photoionization. This is discussed in appendix B through a 3D fluid model that considers stochastic photoionization.

4. Conclusion

In this work, the diffusive ionization wave driven by an extremely fast nanosecond overvoltage pulse in gas mixtures with different oxygen concentrations is investigated through combined experimental and simulation work. The roles of photoionization and direct ionization are discussed through a validated software package (*PASSKEy*).

The ionization wave shares a similar morphology in the experiment and simulation results in all N_2/O_2 mixtures we studied (20%, 2%, 0.2%, 1 ppm, and pure nitrogen): first, it propagates with a spherical shape after its inception then forms a conical when it propagates to nearly half of the gap. During both spherical and conical propagation stages, the ionization wave velocity and width gradually increase until it reaches the plane electrode. Meanwhile, both simulation and experiment results show that with the decrease of the oxygen concentration as well as the photoionization strength in the gas mixtures, the average ionization wave velocity and maximum width decrease slightly, but do not decrease as much as observed in the inception cloud or filamentary streamers, proving the positive ionization wave is strongly controlled by the direct ionization process. By replacing $E_k = 32$ kV cm^{-1} with $E = 180$–205 kV cm^{-1} in the inception cloud diameter estimation function $D = 2\ U\ E^{-1}$, the width of the diffusive ionization wave in 20% mixture during its spherical is also estimated and achieved good agreements with the 2D calculation results.

However, there are two limitations of this work we have to note: First, the conclusions on the atmospheric pressure are mainly based on simulation work, though low-pressure experiment and simulation achieved good agreement, atmospheric pressure experiment in N_2/O_2 mixtures is still needed in the future for further comparison. Second, there is a time difference (1.5 ns) between the ionization wave connection time in the low-pressure nitrogen simulation and experiment, and for diffusive ionization wave, this time difference is relatively large.

The above results that show the positive diffusive ionization wave does not tend to branch in various gas mixtures, combined with its characteristic that can produce excited and reactive species, show the positive diffusive ionization wave might have great potential in plasma-assisted combustion. A study on the repetitive diffuse discharges in combustible mixtures might is as well needed in the future to further explore its application potential.

Data availability statement

The data that support the findings of this study are available upon reasonable request from the authors.

Acknowledgments

This work was supported by the National Natural Science Foundation of China (Nos. 52077169, 51777164), State Key Laboratory of Electrical Insulation and Power Equipment (EIPE22116) and HPC Platform, Xi'an Jiaotong University. We would also like to thank the anonymous referees for their valuable suggestions.

Appendix A. Reactions in the 2D model

Table A1. Reactions considered in the 2D fluid model.

	Reaction	Rate Constant[a]	References
R1	$e + N_2 \rightarrow N_2^+ + e + e$	$f(\sigma, \varepsilon)$	[54]
R2	$e + O_2 \rightarrow O_2^+ + e + e$	$f(\sigma, \varepsilon)$	[55]
R3	$e + N_2 \rightarrow e + N_2(A^3\Sigma_u)$	$f(\sigma, \varepsilon)$	[54]
R4	$e + N_2 \rightarrow e + N_2(B^3\Pi_g)$	$f(\sigma, \varepsilon)$	[54]
R5	$e + N_2 \rightarrow e + N_2(C^3\Pi_u)$	$f(\sigma, \varepsilon)$	[54]
R6	$e + O_2 \rightarrow e + O + O + 0.8$ eV	$f(\sigma, \varepsilon)$	[48, 55]
R7	$e + O_2 \rightarrow e + O + O(^1D) + 1.26$ eV	$f(\sigma, \varepsilon)$	[48, 55]
R8	$N_2^+ + N_2 + M \rightarrow N_4^+ + M + 1.057$ eV	5×10^{-29}	[47, 48]
R9	$N_4^+ + O_2 \rightarrow O_2^+ + N_2 + N_2 + 2.453$ eV	2.5×10^{-10}	[47, 48]
R10	$N_2^+ + O_2 \rightarrow O_2^+ + N_2 + 3.51$ eV	6×10^{-11}	[47, 48]
R11	$O_2^+ + N_2 + N_2 \rightarrow O_2^+N_2 + N_2$	9×10^{-31}	[47]
R12	$O_2^+N_2 + N_2 \rightarrow O_2^+ + N_2 + N_2$	4.3×10^{-10}	[47]
R13	O_2^+ N2$+ O_2 \rightarrow O_4^+ + N_2$	1×10^{-9}	[47]
R14	$O_2^+ + O_2 + M \rightarrow O_4^+ + M + 0.425$ eV	2.4×10^{-30}	[47, 48]
R15	$e + O_2 + O_2 \rightarrow O_2^- + O_2$	$2 \times 10^{-29} \times (300/T_e)$	[47]
R16	$e + O_2 \rightarrow O^- + O$	$f(\sigma, \varepsilon)$	[55]
R17	$O^- + O \rightarrow O_2 + e$	5×10^{-10}	[56]
R18	$O_2^- + O \rightarrow O_2 + O + e$	1.5×10^{-10}	[56]
R19	$e + N_4^+ \rightarrow N_2 + N_2(C^3\Pi_u) + 3.49$ eV	$2 \times 10^{-6} \times (300/T_e)^{0.5}$	[48]
R20	$e + N_2^+ \rightarrow N + N + 2.25$ eV	$2.8 \times 10^{-7} \times (300/T_e)^{0.5}$	[56]
R21	$e + O_4^+ \rightarrow O + O + O_2 + 4.6$ eV	$1.4 \times 10^{-6} \times (300/T_e)^{0.5}$	[47, 48]
R22	$e + O_2^+ \rightarrow O + O + 5.0$ eV	$2 \times 10^{-7} \times (300/T_e)$	[47, 48]
R23	$O_2^- + O_4^+ \rightarrow O_2 + O_2 + O_2 + 6.5$ eV	1×10^{-7}	[47]
R24	$O_2^- + O_4^+ + M \rightarrow O_2 + O_2 + O_2 + M + 6.5$ eV	$2 \times 10^{-25} \times (300/T_{gas})^{3.2}$	[47]
R25	$O_2^- + O_2^+ + M \rightarrow O_2 + O_2 + M + 7.0$ eV	$2 \times 10^{-25} \times (300/T_{gas})^{3.2}$	[47]
R26	$O^- + N_2^+ \rightarrow O + N + N + 2.25$ eV	1×10^{-7}	[56]
R27	$N_2(C^3\Pi_u) + N_2 \rightarrow N_2(B^3\Pi_g, v) + N_2$	1×10^{-11}	[48]
R28	$N_2(C^3\Pi_u) + O_2 \rightarrow N_2 + O + O(^1D) + 4.83$ eV	3×10^{-10}	[48]
R29	$N_2(C^3\Pi_u) \rightarrow N_2 + hv$	2.38×10^7	[47]
R30	$N_2(B^3\Pi_g) + O_2 \rightarrow N_2 + O + O + 2.35$ eV	3×10^{-10}	[48]
R31	$N_2(B^3\Pi_g) + N_2 \rightarrow N_2(A^3\Sigma_u) + N_2(v)$	1×10^{-11}	[48]
R32	$N_2(A^3\Sigma_u) + O_2 \rightarrow N_2 + O + O + 1.0$ eV	$2.5 \times 10^{-12} \times (T_{gas}/300)^{\circ.5}$	[48]
R33	$O(^1D) + O_2 \rightarrow O + O_2 + 0.33$ eV	$3.3 \times 10^{-11} \times \exp(67/T_{gas})$	[48]
R34	$O(^1D) + N_2 \rightarrow O + N_2 + 1.37$ eV	$1.8 \times 10^{-11} \times \exp(107/T_{gas})$	[48]

[a] Unit of rate constants are s^{-1}, $cm^3\ s^{-1}$, and $cm^6\ s^{-1}$. T_e is the electron temperature calculated based on BOLSIG+ with cross sections indicated in the table, units in K. T_{gas} is the gas temperature calculated from the fluid module in *PASSKEy*, units in K. The energy released in each reaction is taken from [48].

Appendix B. Discussion on the stochastic photoionization

A 3D fluid model is established based on the afivo-streamer framework [57], which considers the stochasticity of photoionization through Monte-Carlo approach. The detailed code description and afivo framework description can be found in [58], and the Monte Carlo photoionization description can be found in [59]. This approach achieved good agreement with the experiments in modeling the branching process of positive streamers [60]. We simulated the 200 mbar pressure case in our experiment. The simulation setup is shown in figure B1.

The applied voltage is the same as used in experiments. The considered reactions are the Phelps' database for N_2 and O_2 [54]. Figures B2(a) and (b) shows the electron density evolution during the discharge and figures B2(c) and (d) shows the ionization length and width comparison between the experiment and simulation during its propagation. Here we must emphasize that to ensure they have the same length after inception, the time in the simulation is advanced by 0.4 ns. The calculated results show a good agreement with the experimental results and no breakup effects are found, showing the formation of conical-shaped discharge in 2D simulation is not due to the limitation of its photoionization even in low oxygen concentration gas mixtures.

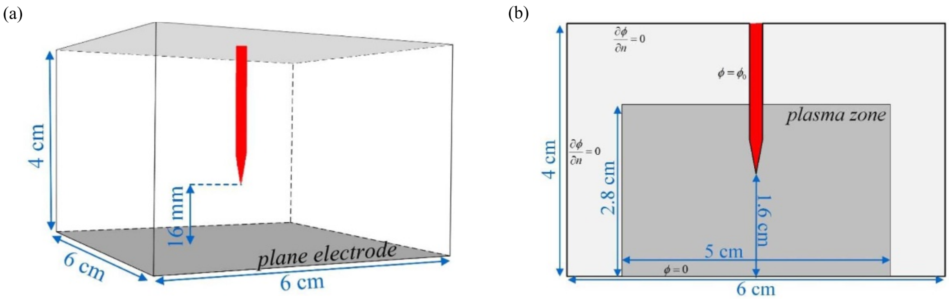

Figure B1. (a). The 3D view of the 3D fluid model. The gap distance between the pin and plane electrode is 16 mm. The pin electrode is colored red. (b). The 2D cross-section view of the 3D fluid model (at $y = 3$ cm). Poisson's equation and photoionization are solved in the whole area, and the continuity equations for species are only solved in the smaller plasma zone (darker-colored area).

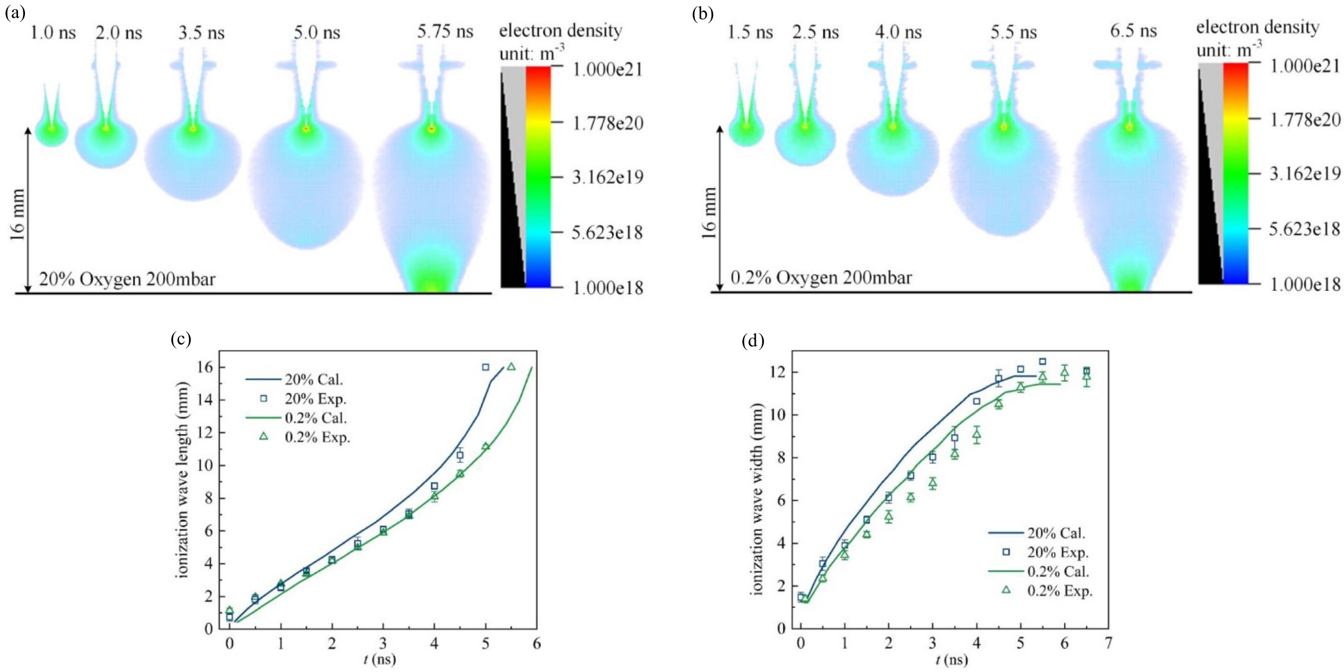

Figure B2. (a). The electron density evolution during the ionization wave propagation in 20% mixture. The colored figures are the cross sections at $y = 3$ cm (50%). (b). The electron density evolution during the ionization wave propagation in 0.2% mixture. The colored figures are the cross sections at $y = 3$ cm (50%). (c). The ionization wave length in the experiment and the 3D calculation. The length is determined by the maximum field at the ionization wave head. Note that to ensure they have the same length when incepts, the time in the simulation is advanced by 0.4 ns. (d). The ionization wave length in the experiment and the 3D calculation. The width is determined by the 10^{18} m^{-3} isoline.

ORCID iDs

Yulin Guo https://orcid.org/0000-0003-0797-1750
Yifei Zhu https://orcid.org/0000-0001-8989-0051

References

[1] Naidis G V, Tarasenko V F, Babaeva N Y and Lomaev M I 2018 *Plasma Sources Sci. Technol.* **27** 013001
[2] Tarasenko V 2020 *Plasma Sources Sci. Technol.* **29** 034001
[3] Babaeva N Y and Naidis G V 2016 *Phys. Plasmas* **23** 703
[4] Tarasenko V F, Beloplotov D V and Lomaev M I 2015 *Plasma Phys. Rep.* **41** 832–46
[5] Beloplotov D V, Tarasenko V F, Lomaev M I and Sorokin D A 2015 *IEEE Trans. Plasma Sci.* **43** 3808–14
[6] Babaeva N Y and Naidis G V 2016 *IEEE Trans. Plasma Sci.* **44** 899–902
[7] Marode E, Dessante P and Tardiveau P 2016 *Plasma Sources Sci. Technol.* **25** 064004
[8] Tardiveau P, Magne L, Marode E, Ouaras K, Jeanney P and Bournonville B 2016 *Plasma Sources Sci. Technol.* **25** 054005
[9] Brisset A, Gazeli K, Magne L, Pasquiers S, Jeanney P, Marode E and Tardiveau P 2019 *Plasma Sources Sci. Technol.* **28** 055016
[10] Chng T L, Brisset A, Jeanney P, Starikovskaia S M, Adamovich I V and Tardiveau P 2019 *Plasma Sources Sci. Technol.* **28** 09LT02
[11] Chng T L, Orel I S, Starikovskaia S M and Adamovich I V 2019 *Plasma Sources Sci. Technol.* **28** 045004
[12] Zhu Y F, Chen X C, Wu Y, Hao J B, Ma X G, Lu P F and Tardiveau P 2021 *Plasma Sources Sci. Technol.* **30** 075025

[13] Bourdon A, Péchereau F, Tholin F and Bonaventura Z 2021 *J. Phys. D: Appl. Phys.* **54** 075204
[14] Chng T L, Pai D Z, Guaitella O, Starikovskaia S M and Bourdon A 2022 *Plasma Sources Sci. Technol.* **31** 015010
[15] Komuro A, Ryu T, Yoshino A, Namihira T, Wang D Y and Ono R 2021 *J. Phys. D: Appl. Phys.* **54** 364004
[16] Ono R and Komuro A 2019 *J. Phys. D: Appl. Phys.* **53** 035202
[17] Namihira T, Wang D, Katsuki S, Hackam R and Akiyama H 2003 *IEEE Trans. Plasma Sci.* **31** 1091–4
[18] Bourdon A, Pechereau F, Tholin F and Bonaventura Z 2021 *Plasma Sources Sci. Technol.* **30** 105022
[19] Nijdam S, Teunissen J and Ebert U 2020 *Plasma Sources Sci. Technol.* **29** 103001
[20] Chen S, Heijmans L C J, Zeng R, Nijdam S and Ebert U 2015 *J. Phys. D: Appl. Phys.* **48** 175201
[21] Nijdam S, van de Wetering F M J H, Blanc R, Veldhuizen E V and Ebert U 2010 *J. Phys. D: Appl. Phys.* **43** 145204
[22] Briels T M P, van Veldhuizen E M and Ebert U 2008 *J. Phys. D: Appl. Phys.* **41** 234008
[23] Pancheshnyi S V, Starikovskaia S M and Starikovskii A Y 2001 *J. Phys. D: Appl. Phys.* **34** 105–15
[24] Zhang X, Guo Y L, Mirpour S, Li Y R, Sun A B and Nijdam S 2021 *J. Phys. D: Appl. Phys.* **54** 485202
[25] Yi W J and Williams P F 2002 *J. Phys. D: Appl. Phys.* **35** 205–18
[26] Wormeester G, Pancheshnyi S, Luque A, Nijdam S and Ebert U 2010 *J. Phys. D: Appl. Phys.* **43** 505201
[27] Teunissen J and Ebert U 2016 *Plasma Sources Sci. Technol.* **25** 044005
[28] Naidis G V 2019 *Plasma Res. Express* **1** 017001
[29] Beloplotov D V, Tarasenko V F, Sorokin D A and Lomaev M I 2017 *JERP Lett.* **106** 653–8
[30] Beloplotov D V, Grishkov A A, Sorokin D A and Shklyaev V A 2021 *Russ. Phys. J.* **64** 340–7
[31] Zhu Y F, Shcherbanev S, Baron B and Starikovskaia S 2017 *Plasma Sources Sci. Technol.* **26** 125004
[32] Zhu Y F and Starikovskaia S 2018 *Plasma Sources Sci. Technol.* **27** 124007
[33] Zhu Y F, Wu Y, Wei B, Xu H J, Liang H, Jia M, Song H M and Li Y H 2020 *J. Phys. D: Appl. Phys.* **53** 145205
[34] Li C, Brok W J M, Ebert U and van der Mullen J 2007 *J. Appl. Phys.* **101** 123305
[35] Grubert G K, Becker M M and Loffhagen D 2009 *Phys. Rev.* E **80** 036405
[36] Piskin T, Podolsky V A, Macheret S O and Poggie J 2019 *J. Phys. D: Appl. Phys.* **52** 304002
[37] Bourdon A, Pasko V P, Liu N Y, Celestin S, Segur P and Marode E 2007 *Plasma Sources Sci. Technol.* **16** 656–78
[38] Pancheshnyi S 2015 *Plasma Sources Sci. Technol.* **24** 015023
[39] Fennelly J A and Torr D G 1992 *At. Data Nucl. Data Tables* **51** 321–63
[40] Ajello J M and Franklin B 1985 *J. Chem. Phys.* **82** 2519–28
[41] Ajello J M, James G K, Franklin B O and Shemansky D E 1989 *Phys. Rev.* A **40** 3524–56
[42] Zhu Y F, Wu Y and Li J Z 2020 (arXiv 2005.10021)
[43] Zheleznyak M B, Mnatsakanyan A K and Sizykh S V 1982 *High Temp.* **20** 357–62
[44] Janalizadeh R and Pasko V P 2019 *Plasma Sources Sci. Technol.* **28** 105006
[45] Penney G W and Hummert G T 1970 *J. Appl. Phys.* **41** 572-&
[46] Przybylski A 1961 *Z. Naturforsch* A **16** 1232–7
[47] Pancheshnyi S, Nudnova M and Starikovskii A 2005 *Phys. Rev.* E **71** 016407
[48] Popov N A 2011 *J. Phys. D: Appl. Phys.* **44** 285201
[49] Pechereau F, Le Delliou P, Jansky J, Tardiveau P, Pasquiers S and Bourdon A 2014 *IEEE Trans. Plasma Sci.* **42** 2346–7
[50] Briels T M P, Kos J, Winands G J J, van Veldhuizen E M and Ebert U 2008 *J. Phys. D: Appl. Phys.* **41** 234004
[51] Komuro A, Ono R and Oda T 2013 *Plasma Sources Sci. Technol.* **22** 045002
[52] Li Y, van Veldhuizen E M, Zhang G J, Ebert U and Nijdam S 2018 *Plasma Sources Sci. Technol.* **27** 125003
[53] Li X R, Dijcks S, Nijdam S, Sun A B, Ebert U and Teunissen J 2021 *Plasma Sources Sci. Technol.* **30** 095002
[54] Phelps A V and Pitchford L C 1985 *Phys. Rev.* A **31** 2932–49
[55] Lawton S A and Phelps A V 1978 *J. Chem. Phys.* **69** 1055–68
[56] Kossyi I A, Kostinsky A Y, Matveyev A A and Silakov V P 1992 *Plasma Sources Sci. Technol.* **1** 207–20
[57] Teunissen J and Ebert U 2017 *J. Phys. D: Appl. Phys.* **50** 474001
[58] Teunissen J and Ebert U 2018 *Comput. Phys. Commun.* **233** 156–66
[59] Bagheri B and Teunissen J 2019 *Plasma Sources Sci. Technol.* **28** 045013
[60] Wang Z, Dijcks S, Guo Y, van der Leegte M, Sun A, Ebert U, Nijdam S and Teunissen J 2022 (arXiv:2208.07279)